VIRTUAL IMAGING FRAMEWORK OF DYNAMIC PHOTOACOUSTIC COMPUTED TOMOGRAPHY FOR SMALL ANIMALS

By

James Soole

Senior Thesis in Computer Engineering

University of Illinois at Urbana-Champaign

Advisor: Mark A. Anastasio

May 2022

Abstract

Photoacoustic Computed Tomography (PACT) is a biomedical imaging modality used to acquire images of biological tissue and structures with a combination of optical and ultrasound techniques, avoiding ionizing radiation and the need to excise tissue. Dynamic PACT, using multiple sequential PACT images, can provide a method for visualizing biological material movement and physiological changes throughout a tissue over time. However, it can be very inefficient to assess and optimize imaging systems through clinical trials. Virtual Imaging Trials (VIT) offer an alternative: simulation. With computational models of imaging systems and objects, VITs can more cheaply and efficiently emulate a real-world PACT imaging system.

This thesis describes the creation of a framework of dynamic PACT imaging simulations for small animals, simulating photon transport and acoustic wave propagation to produce simulated acoustic pressure measurements. The developed framework can be used for simulation of static and dynamic objects, with parameters easily updated to reflect the geometry of varied target imaging systems. Simulated output pressure measurements from this framework have been validated for static and dynamic imaging cases, producing outputs similar to those of their experimental counterparts.

This framework creates a basis for running varied virtual trials of dynamic PACT imaging, allowing for use with different imaging systems and numerical phantoms. A user can run simulations with numerical phantoms of different sizes and shapes or optical and acoustic properties and can adjust illumination and measurement geometry to match that of the target imaging system they are emulating.

Subject Keywords: photoacoustic computed tomography; PACT; dynamic PACT; virtual imaging trials; biomedical imaging

Acknowledgments

I would like to thank my advisor, Professor Mark A. Anastasio, for letting me work on my senior thesis in his lab. I would also like to thank Seonyeong Park and Refik Mert Cam for their indispensable help navigating through such a well-structured and engaging project.

Contents

1. Introduction 1
2. Literature Review 3
2.1 PACT 3
2.2 Virtual Imaging Trials for PACT 4
2.3 Numerical Mouse Phantoms 5
3. Virtual Imaging Framework of 3D Dynamic PACT for Small Animals 7
3.1 Dynamic Mouse Phantoms and Property Assignment 7
3.2 Simulation of Photon Transport 8
3.3 Simulation of Acoustic Wave Propagation 11
4. Results and Validation 13
4.1 Numerical Simulation Results 13
4.2 Validation 18
4.2.1 Static X-shaped Tube Phantom 18
4.2.2 Dynamic Tube Phantom 19
5. Conclusion 21
References 22
Appendix A Phantom Labeling Table 25

1. Introduction

Photoacoustic Computed Tomography (PACT), also known as thermoacoustic tomography (TAT) or optoacoustic tomography (OAT), is a biomedical imaging modality used to acquire images of biological tissue and structures with a combination of optical and ultrasound techniques [1]-[3]. In PACT, an object such as biological tissue is irradiated by a laser beam at a near-infrared (NIR) wavelength. This tissue converts the absorbed radiation into heat energy and expands, creating broadband ultrasound signals that are measured by transducers at multiple locations outside the tissue. The ultrasound measurement data is then used by an image reconstruction algorithm to produce a map of initial pressure distribution within the object that is proportional to the absorbed optical energy density [2]. This technique avoids excising tissue and ionizing radiation, using laser light at NIR wavelengths which can be specifically chosen to target endogenous or exogenous contrast agents: hemoglobin, lipid, melanin, or other biologically relevant materials. Dynamic PACT involves the use of PACT over several sequential time steps, allowing for the visualization of dynamic physiological event and medicine tracking throughout a tissue over time [4]-[5].

When developing a new imaging system, candidate designs should be evaluated and optimized. Given that imaging systems have a large number of parameters, it is very inefficient if not impossible to adequately assess and optimize with physical clinical trials. They can be time-consuming and expensive, and may also raise some ethical concerns. Virtual Imaging Trials (VITs), or in-silico imaging trials, can be an alternative. VITs provide a framework to facilitate experimentation with, assessment, and optimization of imaging methods with computational models of imaging systems and objects [6]. In simulation, one can produce imaging data more quickly and cheaply than doing so physically, easily changing parameters of an imaging system that would be challenging to do so for an already-realized physical system. VITs also require the use of digital imaging phantoms, a representation of the physical tissue or object to be imaged.

The focus of this thesis is to create a framework of dynamic PACT imaging simulations for small animals, that includes generation of numerical mouse phantom, optical and acoustic property assignment, and simulations of photon transport and acoustic wave propagation. The framework allows for easy modification to system parameters, including the choice of numerical phantom used, phantom labeling schemes, assigned optical and acoustic properties, and physical configuration of the imaging system. The framework can be used for simulations of both static and dynamic objects.

The remainder of this paper is organized as follows. In Section 2, we review the existing literature on PACT, VITs, and numerical phantoms. The numerical mouse phantoms used by the framework, optical and acoustic property assignment, and illumination and measurement geometry configurations of simulation are described in Section 3. Numerical simulation and validation results are presented in Section 4. The conclusion of the study is provided in Section 5.

2. Literature Review

2.1 PACT

The PACT image formation can be broken into four steps. Initially, the object is illuminated with an optical pulse. NIR light can penetrate further into an object than mid-infrared radiation, and specific NIR wavelengths can be chosen to target relevant endogenous or exogeneous contrast agents. Then, the object generates an initial pressure distribution in accordance with the photoacoustic effect [3]. The photoacoustic effect is the formation of sound waves following light absorption in a material sample. We can calculate the induced initial pressure wavefield according to

$$p(\boldsymbol{r}, t = 0) = \Gamma \, \mu_a(\boldsymbol{r}) \, \Phi_s(\boldsymbol{r}) \quad , \tag{1}$$

where $\boldsymbol{r} \in \mathbb{R}^3$ is the spatial location, μ_a is the optical absorption coefficient, Φ_s is the optical fluence, and Γ is the Grüneisen parameter, a measure of efficiency in energy conversion (optical to mechanical) [3]. Fluence, or radiant exposure, is the radiant energy received by a surface per unit area, or equivalently the irradiance of a surface, integrated over time of irradiation [7].

Subsequently, the sound (pressure) waves, formed by the photoacoustic effect, propagate from the object. This propagated pressure is measured by surrounding piezoelectric sensors, devices used to measure changes in pressure by converting them to electrical charge. In this paper they are also referred to by the more general term “transducer.”

Lastly, these recorded pressure measurements can be used to reconstruct an image of the object, serving as input to an inversion problem.

Dynamic PACT involves the use of multiple sequential PACT images over a period of time, allowing for the visualization of biological material movement and physiological changes throughout a tissue. It can be used to observe motion of biologically relevant materials like hemoglobin as well as exogenous contrast agents.

2.2 Virtual Imaging Trials for PACT

There has been research conducted on VITs for a number of imaging modalities and objects [6]. They have been used to examine X-ray imaging of human breasts using Monte Carlo simulation [8], with frameworks intended for optimization of scanning design [9]. Monte Carlo simulations have also been used on mice, for medicine tracking [10], neural-net-optimized micro-CT imaging [11], and organ-specific PACT analysis [12].

There has also been research conducted on creating realistic numerical phantoms of animal bodies and human breast tissue [13] for use in PACT VITs. Open-source software simulation tools such as k-Wave [14] have been used to model imaging systems with these phantoms [15,16]. K-wave specifically has been used in PACT studies for simulation of acoustic wave propagation [12,17].

However, there has been less focus on providing a universal framework to use these phantoms in simulation [2,18], and there has been no framework for dynamic PACT. A framework for these imaging trials requires simulation of the imaging methods that PACT employs. To simulate photon transport and acoustic wave propagation, we can use software tools such as MCXLAB [12,19] and k-Wave [14], respectively, or other equivalent tools.

2.3 Numerical Mouse Phantoms

Running a PACT simulation requires the use of a numerical phantom, a digital representation of the object to be imaged. There have been multiple realistic mouse phantoms created, notably the static Atlas mouse phantom and the dynamic MOBY phantom [20,21]. The Atlas mouse phantom is a numerically-labeled 3D murine model with specified labels of organ/tissue types at each voxel (3D equivalent of pixel) [20]. Maximum Intensity Projections (MIPs) of the phantom are shown in Figure 1. The phantom was developed by a UCLA group using a training set of micro-CT images and can be deformed into various body poses and weights, appropriately deforming its 89 internal organs.

The MOBY mouse phantom is a 4D labeled murine phantom capable of modeling time-dependent cardiac and respiratory motions [21]. MIPs of the phantom, containing 78 labeled organs, are shown in Figure 2. The phantom was developed by a Johns Hopkins University group using high-resolution 3D magnetic resonance microscopy. Before creation, a user can specify for the phantom to exhibit no motion, heart beating motion (heart beating or contraction), respiratory motion (organ motion due to breathing), or both.

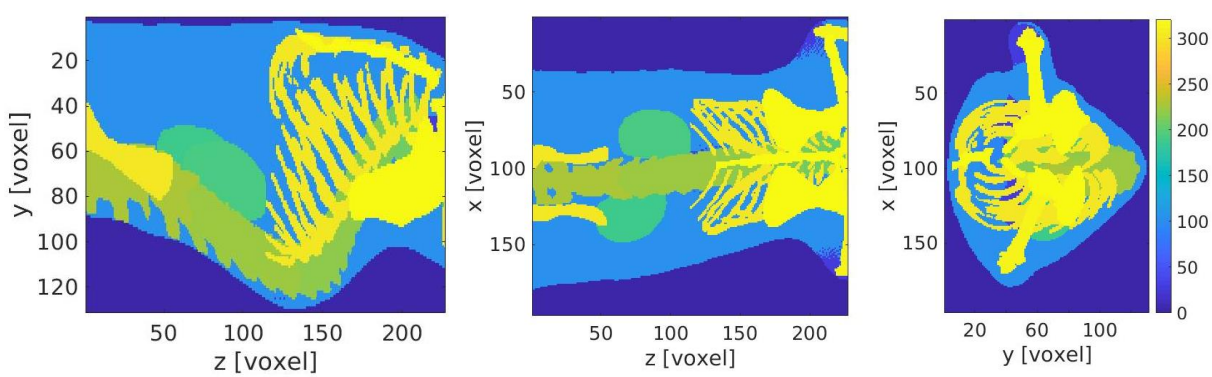

Figure 1 MIPs of Atlas mouse phantom along x-axis (left), y-axis (center), and z-axis (right).

Normal cycle durations are 1 s and 5 s, respectively, though they can be set to any value. A user can specify the motion type, cycle length(s), number of frames/time-steps, and frame interval. Phantom generation produces specified frames of the 3D phantom at subsequent timesteps in separate binary files. These 3D phantoms are generated non-stochastically for consistent motion parameters, with varied organ locations across timesteps according to the type of motion specified.

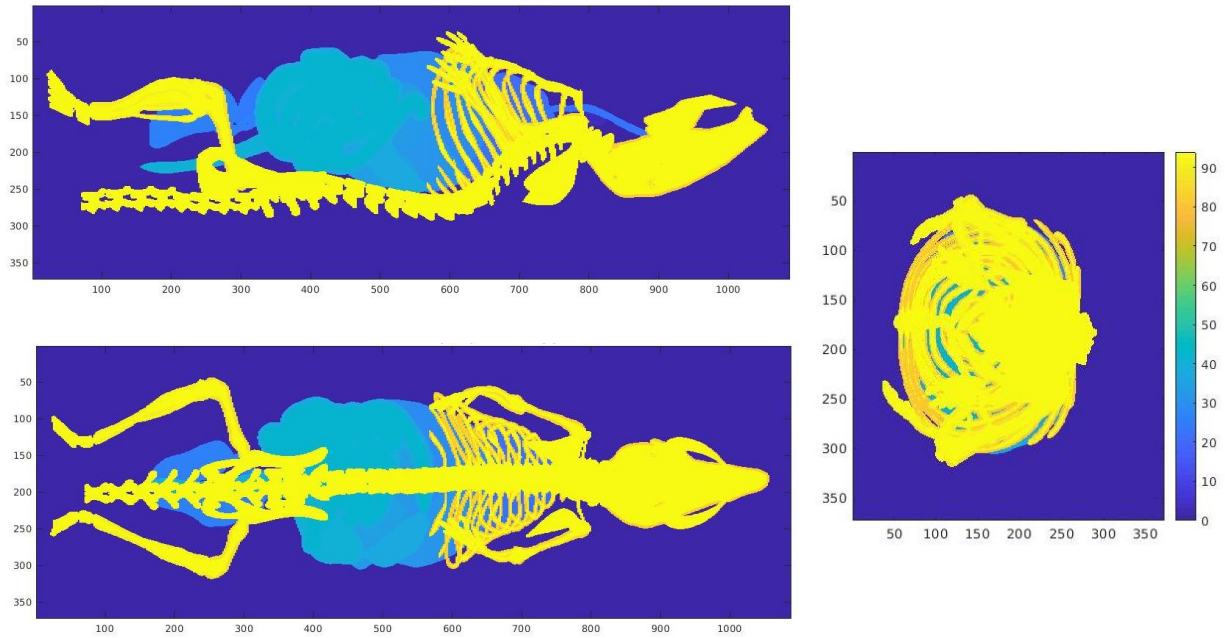

Figure 2 MIPs of MOBY mouse along x-axis (top), y-axis (bottom), and z-axis (right).

3. Virtual Imaging Framework of 3D Dynamic PACT for Small Animals

In the framework, the target imaging system and phantom used can be configured by user's choice. In this thesis, we chose to use the dynamic MOBY phantom. Optical and acoustic properties of the mouse phantom were assigned in accordance with tissue types. For simulations of photon transport and acoustic wave propagation, we mimicked the TriTom Imaging System by PhotoSound Technologies, Inc. [22,23]. All of the PACT simulation discussed in this paper were conducted in MATLAB.

3.1 Dynamic Mouse Phantoms and Property Assignment

In simulation, we use a numerical mouse phantom as the object, assigning its optical and acoustic properties based on literature. The framework considers the use of both the static Atlas phantom and the dynamic MOBY phantom. For compatible use of the two phantoms (which have different labels), each tissue type of the phantoms was given a new "assigned" label. Tissues common to multiple phantoms use the same label. These label assignments, along with corresponding optical properties, are given in Appendix A.

When conducting a dynamic simulation, these properties of the phantom can change over time, both in the value of a specific optical property and in the phantom's structure, i.e., the locations of its organs. In this thesis we used the MOBY phantom, which incorporates structural motion as specified for in its configuration file. We used both motions, respiratory and heart beating, with a frame interval of 1 s and normal cycles of 5 s and 1 s, respectively. We chose to produce 36 frames of the phantom at a voxel size of 0.1 mm.

The other dynamic aspect of a phantom is that the optical property changes due to physiological events. Before running an optical simulation with MCXLAB, we must specify four optical properties for each organ/tissue type of the phantom: absorption coefficient μ_a, scattering coefficient μ_s, anisotropy g, and refractive index n. We set all but one of these properties to a constant value for each organ type during simulation. We choose to alter μ_a of a single organ as PACT employs a contrast mechanism based on optical absorption (eq. 1) [13]. The kidney was specifically chosen as a target organ because it is a large, blood-containing organ, as hemoglobin is a major endogenous contrast agent at NIR wavelengths. We

varied μ_a of the phantom's kidney sinusoidally with time, reaching a minimum of the standard coefficient value and a maximum of twice that value.

Using the phantom's tissue labeling (Appendix A), we assigned the optical property values for each organ type in accordance with data from literature [24]-[26]. For tissue types present in the phantom and included in the literature, i.e., "pancreas" in both, property values were directly used. For phantom tissue types not included in the literature, their properties were assigned to that of the most similar given tissue type, for example using the properties of "liver" for the phantom's "gallbladder", or "skeleton" for "left scapula". These optical property values can be set by user's choice.

Likewise, for a k-Wave acoustic simulation, we must assign the acoustic properties sound speed c, density ρ, acoustic attenuation coefficient α, and attenuation power law exponent y. The first three properties were assigned from values given by The Foundation for Research on Information Technologies in Society (IT'IS) [27]-[29], again assigning properties for similar tissues if the phantom's tissue is not included in the database. The power law exponent was set at a constant value of 1.5 for all tissues.

3.2 Simulation of Photon Transport

To simulate photon transport, we use MCXLAB. MCX is a GPU-accelerated open-source light transport simulator, with MCXLAB being the native MEX version of MCX for MATLAB, meaning the entirety of MCX simulation code is compiled into a single MEX function that can be called directly in MATLAB.

The target imaging system, TriTom imaging system [22,23], has three compartments, as illustrated in Figure 3. An anesthetized mouse is located within an animal restrainer unit (6 in Figure 3), and it is lowered into a water tank (1 in Figure 3) together with a photoacoustic array detector (i.e., transducer arc, 3 of Figure 3). The restrainer unit rotates in discrete steps. At each step, the mouse is illuminated by four fiber optic illuminators attached to the surface of the water tank (2 of Figure 3), two for orthogonal excitation and two for epi-illumination. In this framework, only orthogonal excitation is simulated. Then the generated acoustic pressure propagates and is measured at the photoacoustic array detector (3 of Figure 3).

The optical illumination geometry for simulation mimics a simplified geometry of the TriTom system, as shown in Figure 4. Dimensions of the tank, optical fibers, and transducers are included in the figure. Optical fibers are set for orthogonal illumination, positioned 180 degrees apart, each 90 degrees from the transducer arc. TriTom illuminators are linearly-shaped, and light is propagated cylindrically. However, MCXLAB is limited in light source types and cannot simulate such geometry. We instead simulate each illuminator using five cone-shaped beams evenly distributed along the linear optical fiber, each with a half-angle of 16.15 degrees. Using a greater number of cones would lead to more realistic simulation as a tradeoff with computational runtime.

The size of the MCXLAB simulation domain (*cfg.vol*) is 475 × 475 × 400 voxels (190 × 190 × 160 mm^3), which accounts for the diameter (190 mm) and height (160 mm) of the water tank at a voxel size of 0.4 mm. MCXLAB was set to simulate with 1e8 photons (> 475 × 475 × 400), an output type of optical fluence, and a time step of 5e-8 s.

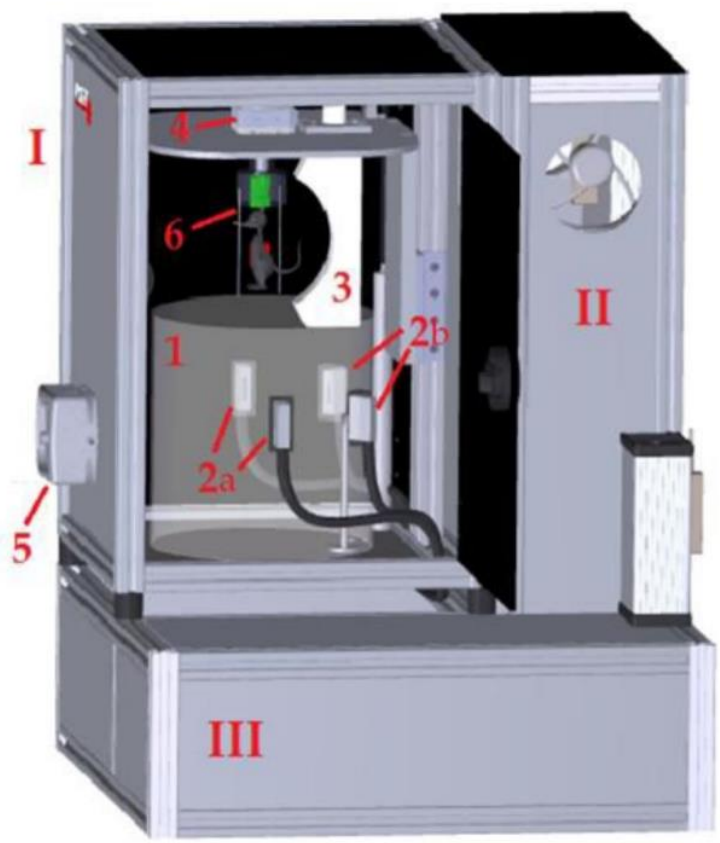

Figure 3 TriTom Imaging System. (I) imaging module, (II) dry electronics compartment, (III) wet compartment. Imaging module consists of: (1) water tank; (2) fiberoptic illuminators (a – orthogonal excitation, b – epi-illumination); (3) photoacoustic array detector; (4) rotary stage; (5) optical detection unit; (6) animal restrainer & anesthesia delivery unit [22].

To mimic rotation of the TriTom's rotary stage (4 of Figure 3), we instead rotated the position of the illuminators (and the transducers), which is functionally equivalent, but more convenient to simulate. Instead of running simulations with the illuminators at each of 360 degrees around the object, we choose to run simulations at only 36 "views", spaced 10 degrees apart, to reduce simulation runtime. TriTom's motor rotates 1 degree every 0.1 seconds, making each view occur 1 second apart in the simulation, prompting the previously-discussed choice to set frame interval to 1 s during MOBY phantom generation. Before simulation, we downsampled each phantom from a voxel size of 0.1 mm to 0.4 mm with nearest-neighbor interpolation. At each view, we used the corresponding frame of MOBY phantom (out of 36), running two simulations (one for each illuminator) and averaging output fluence of the two.

Using the MCXLAB output, i.e., the optical fluence distribution, we calculate an initial pressure distribution according to eq. 1. We assume Γ to be "1," representative of complete efficiency in energy transfer, a common assumption for soft tissue [13,30].

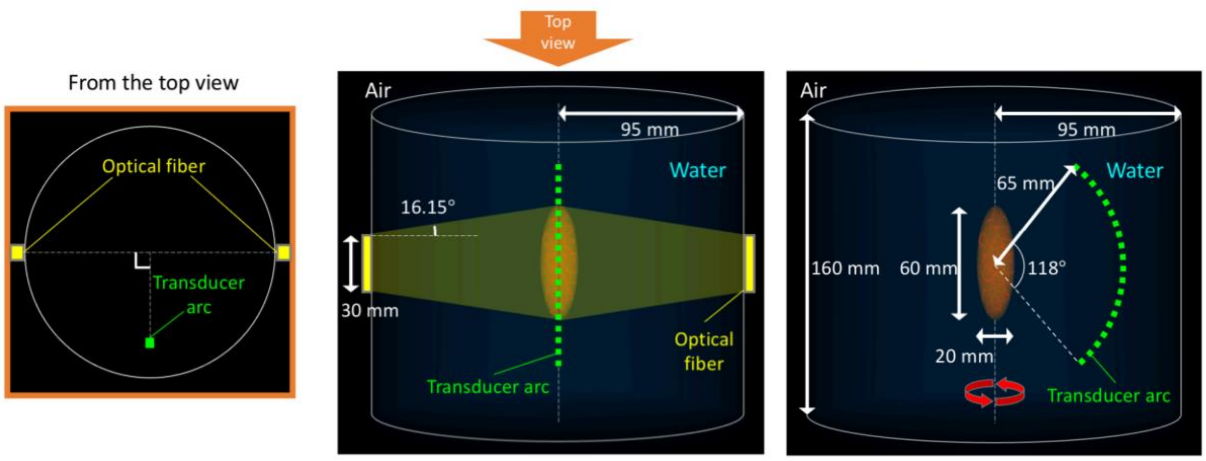

Figure 4 TriTom illumination geometry top view (left) and front view (center). Measurement geometry (right) includes arc of 96 transducers.

3.3 Simulation of Acoustic Wave Propagation

Once we have conducted the optical simulation with MCXLAB, producing simulated optical fluence distribution and subsequently calculating initial pressure distribution, we can conduct simulation of acoustic wave propagation with the GPU-accelerated k-Wave for a given measurement geometry. k-Wave is an open source, third party, MATLAB toolbox designed for the time-domain simulation of propagating acoustic waves. It is a numerical model that can account for heterogeneous material parameters and power law acoustic absorption with linear and nonlinear wave propagation.

Transducer locations (radius, arc angle, arc origin, etc.) were specified as in Figure 4. The transducer arc was composed of 96 individual transducers. The number of time samples was set to 2048 with a sampling rate of 31.25 MHz, the same as with TriTom. Again, we conducted the simulation for a total of 36 tomographic views.

The size of k-Wave simulation domain (*kgrid*) is 680 × 680 × 600 voxels (136 × 136 × 120 mm^3), creating a volume just large enough to include the transducer arc and a Perfectly Matched Layer (PML) on each edge. A PML is an artificial absorbing layer for wave equations, commonly used to truncate computational regions in numerical methods [31]. The simulation domain size along x- and y-axis (136 mm) was greater than double the arc radius (65 mm) in addition to two PMLs of size 10 voxels. The simulation domain size along z-axis was greater than the full vertical height of the arc ($2 * scanning_radius * sin(arc_angle/2)\ /\ voxel_size$) in addition to two PMLs of size 10 voxels. The voxel size was 0.2 mm, the smallest possible size given the 32.48 GB memory usage capacity of the NVIDIA Tesla V100 Pcle GPU used for simulation.

K-wave takes, as input, the assigned acoustic properties (medium) and initial pressure (source). For each of the 36 views, we linearly upsampled the calculated initial pressure distribution from a voxel size of 0.4 mm to 0.2 mm and set it as the source. The photon transport simulation at a coarser grid accompanied with upsampling is equivalent to smoothing of the initial pressure distribution that is required to reduce the amplitudes of the high spatial frequency components in the simulation of acoustic wave propagation. We used different frames of the initial pressure distribution for each tomographic view because the assigned μ_a, and therefore fluence, vary at each view. We then assign appropriate acoustic properties of the phantom and simulation domain (an acoustic coupling medium, i.e., water) to the

medium for that view. Finally, we ran the k-Wave simulation, storing the 96×2048 result (transducer count $\times$ time-step) for each time frame accordingly into the $2048 \times 96 \times 36$ output pressure matrix.

4. Results and Validation

4.1 Numerical Simulation Results

Four successive frames of the MOBY phantom, used for simulation, with noticeable respiratory motion are shown in Figure 5. The following figures were created in MATLAB using a colormap of parula. Figure 5 shows an x-slice of the phantom (integer tissue labels), sized $372 \times 372 \times 1088$ voxels, down the middle at $x = 186$. Because the frame interval and heart beating cycle length were the same, and each frame is produced at the same point in the cycle, heart beating motion is not observed. Individually, respiratory motion was more visible than heart motion.

Figure 6 shows an x-slice of μ_a for the MOBY phantom in successive frames. The slice is taken at $x = 35$ to observe the kidney's time-varying μ_a.

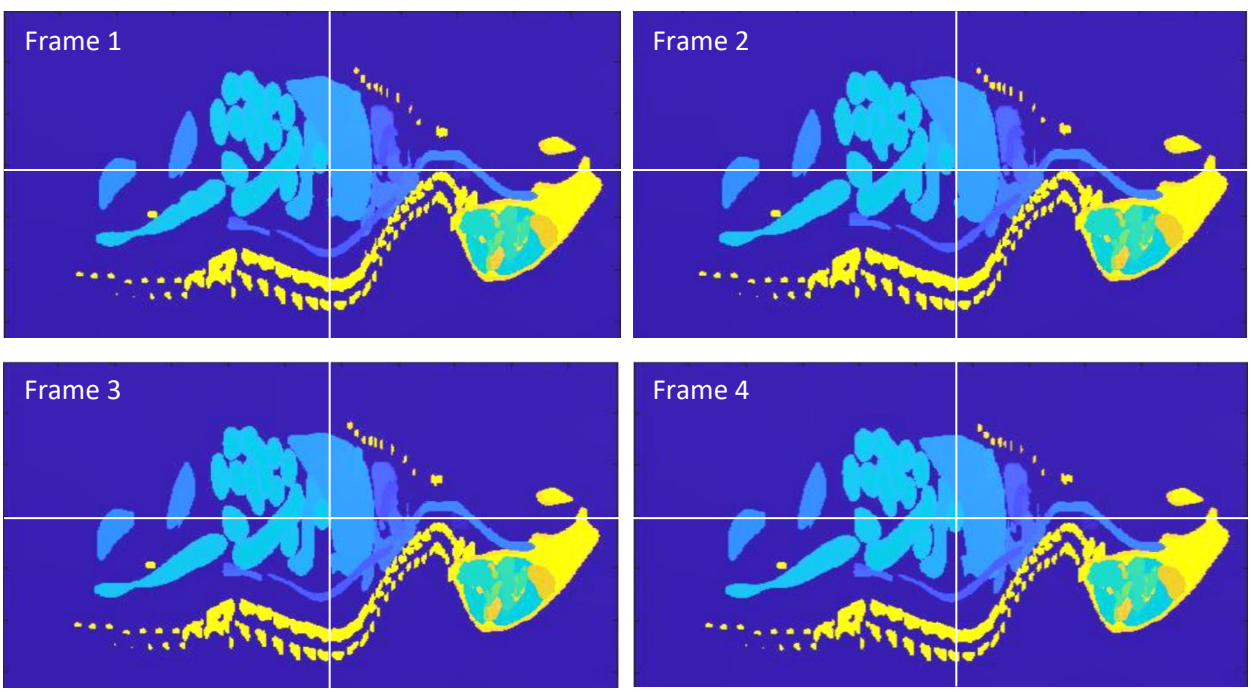

Figure 5 Four successive frames of MOBY phantom tissue labels with Respiratory Motion cycle of 5 s. X-slice at x = 186. An identical grid is in the frames for a comparison of organ positions according to respiratory motion. For example, the boundary of a half bottom of the liver is on the vertical axis in Frames 1 and 2, but it is slightly on the right of the axis in Frames 3 and 4.

A maximum intensity projection map of optical properties μ_a and μ_s values used in this simulation is shown in Figure 7. The assigned anisotropy of all tissue was 0.9, and that of a water background was 0.99. The refractive index of all tissue and a water background was set to 1.37 and 1.33, respectively.

MIPs along x-axis of acoustic properties sound speed (left), density (center), and acoustic attenuation coefficient (right) assigned to MOBY phantom are given in Figure 8. The power law exponent was set at a constant value of 1.5 for all tissues.

The output optical fluence of the photon transport simulation is given in Figures 9 and 10. Each figure shows 9 of 36 illumination views. Figure 9 shows MIPs along z-axis of the simulated optical fluence, i.e., a top-down view of the entire simulation domain, at different frames (i.e., illumination views). As shown in Figure 9, the two opposing illuminators rotated around the object over time. Figure 10 shows MIPs along x-axis of the simulated optical fluence, i.e., a side view of the domain cropped to focus on the phantom, at different frames (i.e., illumination views).

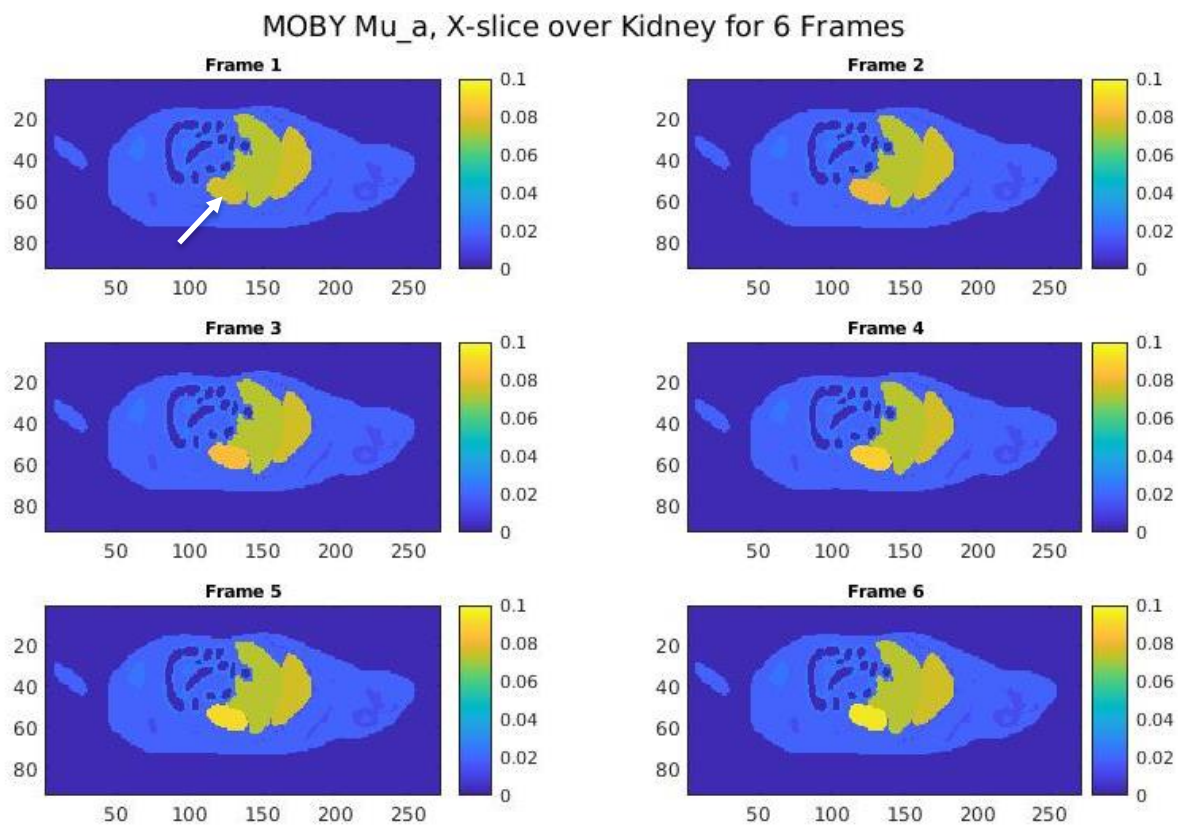

Figure 6 Optical absorption coefficient μ_a [mm^{-1}] map of MOBY phantom tissue in successive frames. Arrow points to kidney. X-slice at x = 35.

The simulated pressure measurements are shown in Figure 11. The 96 transducers, each at 36 different tomographic views, are given on the y-axis "Transducer Location" in Figure 11. Noticeable vertical undulation in pressure values was caused by ordering of transducer measurements, as values vertically adjacent are produced by different transducers, with the result for the bottom-most transducer of one view directly preceding that of the top-most transducer of the next view.

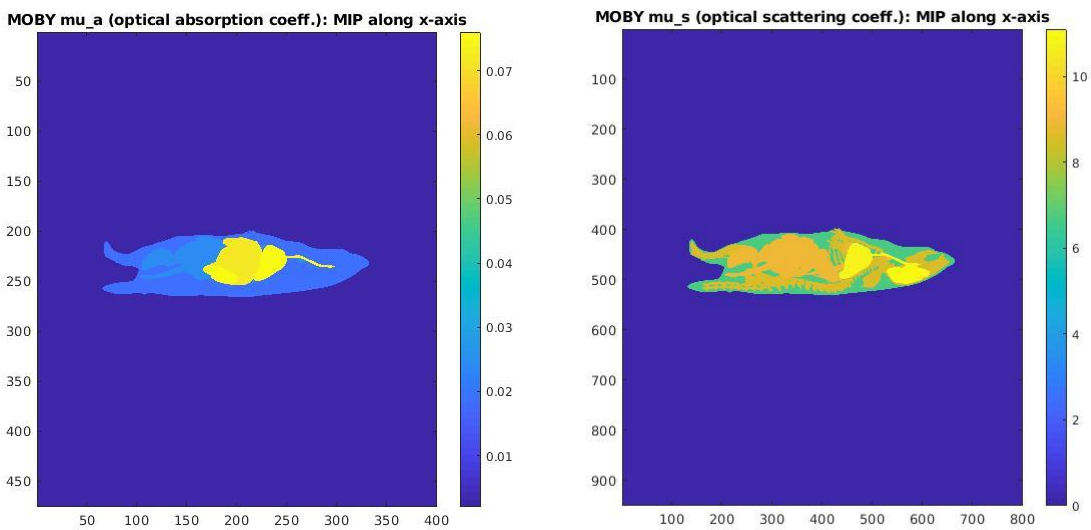

Figure 7 MIPs along x-axis of optical absorption coefficient in mm^{-1} (left) and optical scattering coefficient in mm^{-1} (right) assigned to MOBY phantom.

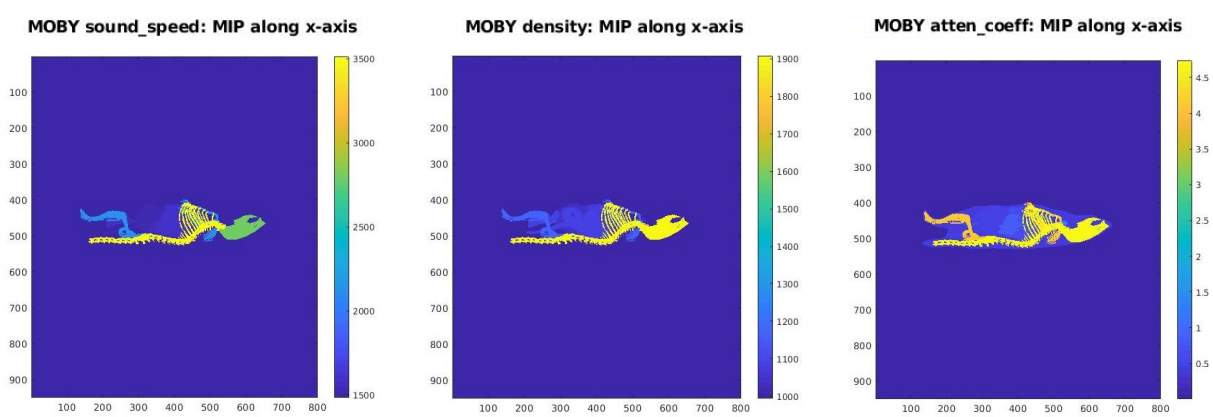

Figure 8 MIPs along x-axis of sound speed in m/s (left), density in kg/m^3 (center), and attenuation coefficient in dB/[cm*MHz] (right) assigned to MOBY phantom.

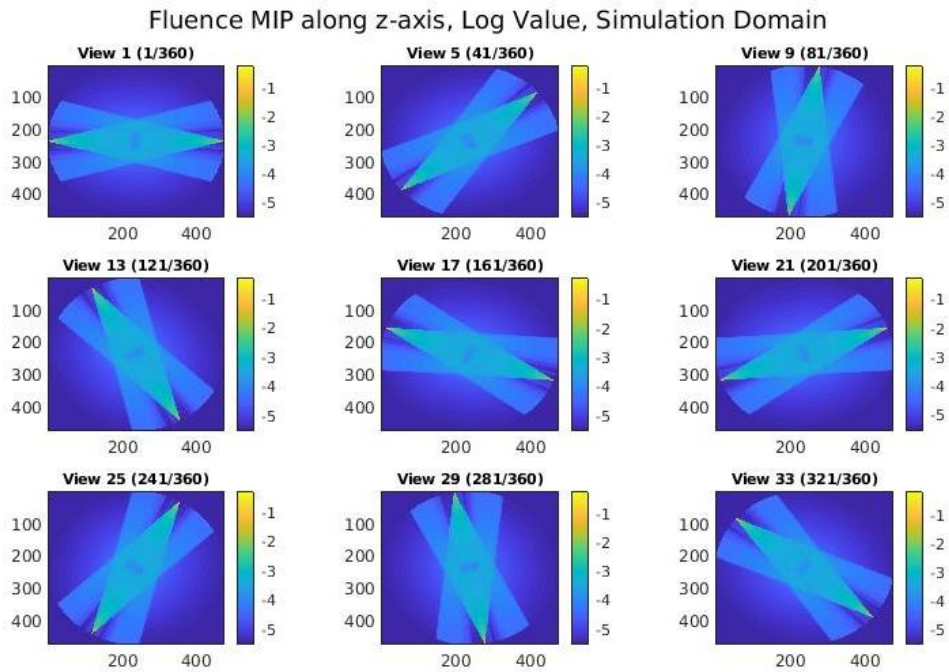

Figure 9 MIPs along z-axis of simulated optical fluence output (entire simulation domain) for 9 of 36 illumination views in a logarithmic scale.

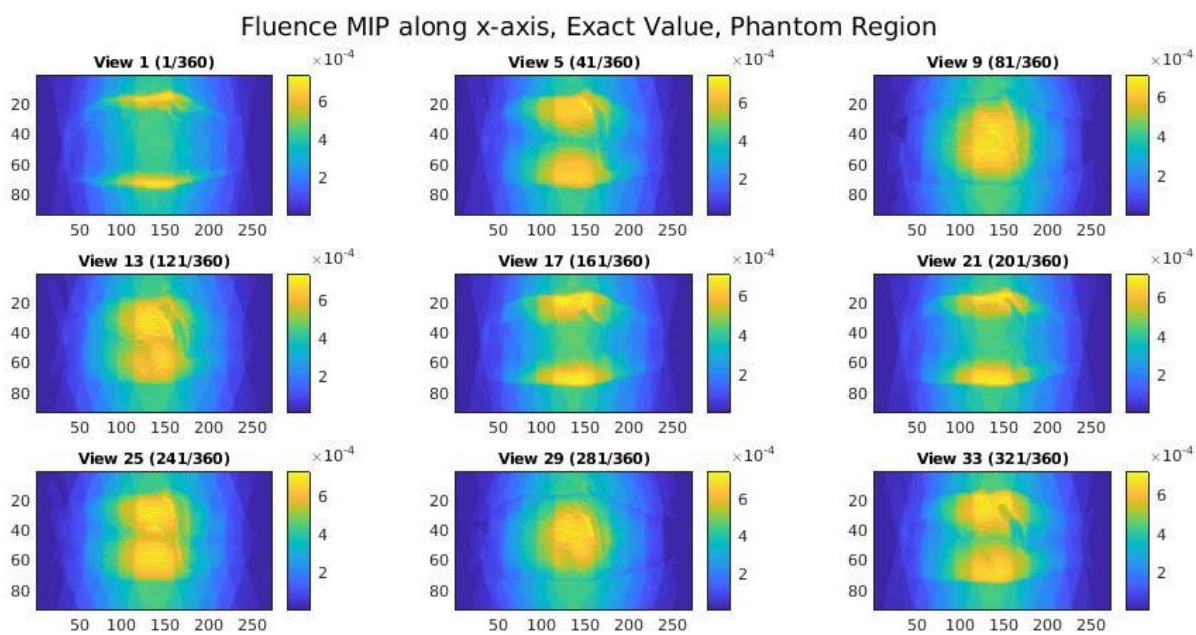

Figure 10 MIPs along x-axis of simulated optical fluence output (phantom region) for 9 of 36 illumination views.

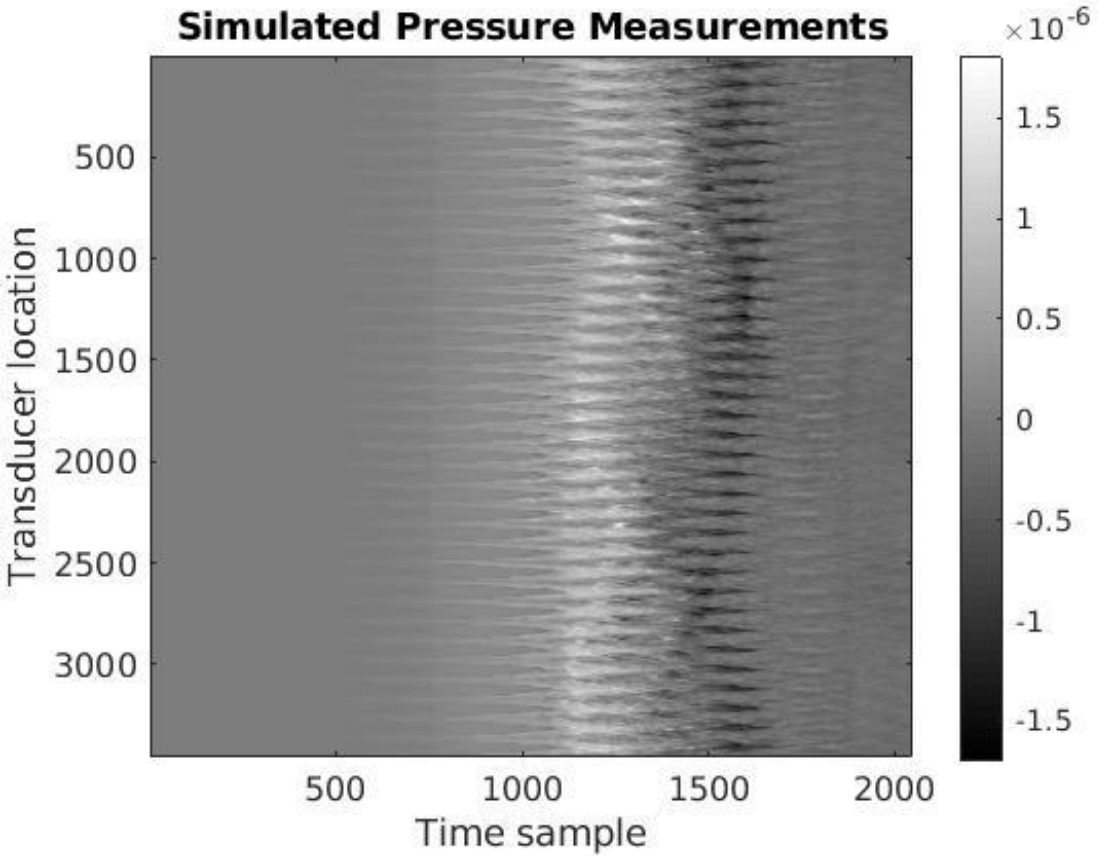

Figure 11 Simulated pressure measurements over time for MOBY phantom. 96 transducers at 36 different views on y-axis. Time sample on x-axis.

4.2 Validation

For validating the efficacy of the simulation framework, we compared our simulated measurements with experimental equivalents for both a static and dynamic case.

4.2.1 Static X-shaped Tube Phantom

Static validation was based on experimental results of an X-shaped tube phantom, as demonstrated by S. A. Ermilov's research [22]. The initial pressure distribution reconstructed from experimental measurements using filtered back-projection was assumed as a true initial pressure distribution in the simulation of acoustic wave propagation. MIPs along x, y, and z-axis of the initial pressure distribution are given in Figure 12. The voxel size was set at 0.2 mm, the number of time samples at 2048, and the sampling rate at 31.25 MHz. Sound speed and density were assumed to be homogeneous, 1506 m/s and 994 kg/m^3 respectively. Acoustic attenuation was not assumed. Experimental and simulated results are given in Figure 13. Experimental measurements were significantly noisy, so they were first given a bandpass filter with a frequency range of 500 kHz – 8 MHz. Its intensity range was set from 10% of minimum to 10% of maximum intensity to show photoacoustic signals. Both results produced a similar ridge at a similar time sample. MCXLAB produces a normalized distribution of optical fluence as output, resulting in an arbitrary (scaled) unit for the simulated pressure values. The given true distribution of initial pressure was given in an arbitrary unit.

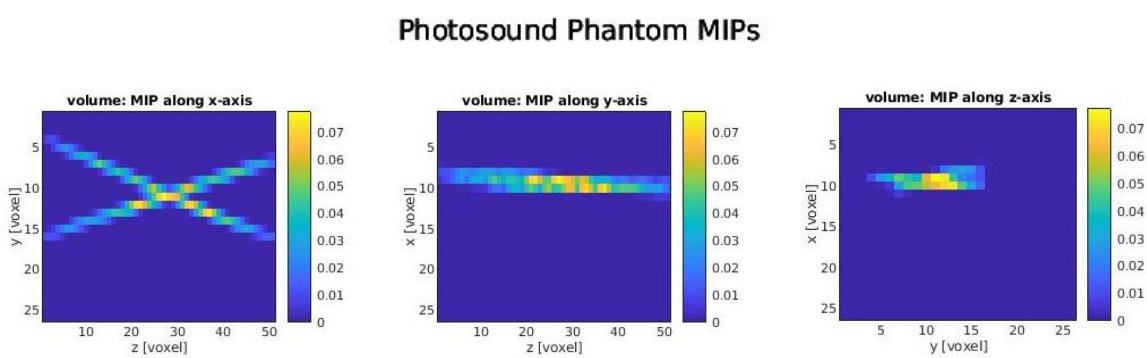

Figure 12 Initial pressure MIPs of Photosound's X-shaped phantom [22] along x-axis (left), y-axis (center), and z-axis (right).

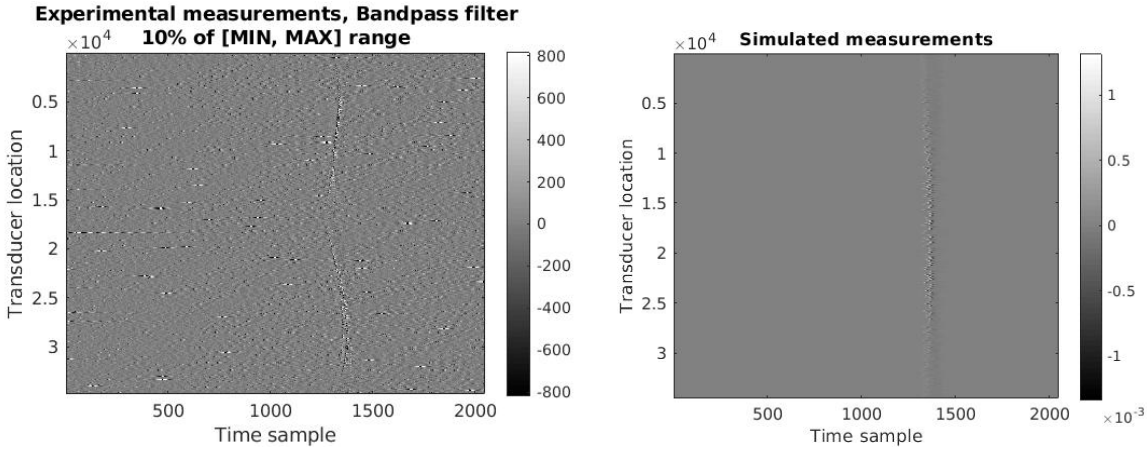

Figure 13 Experimental (left) and simulated (right) measurements of transducer output over time for PhotoSound's X-shaped phantom [22]. Experimental shown after 500 kHz – 8 MHz bandpass filter.

4.2.2 Dynamic Tube Phantom

Dynamic validation was based on experimental results of a tube phantom from PhotoSound measured with the TriTom imaging system. A total of 360 frames of the initial pressure distribution, reconstructed using a dynamic image reconstruction, was assumed to be the true distribution. MIPs along x, y, and z-axis of the last frame of the initial pressure distribution are given in Figure 14. Fluid flowed through the hollow tube, allowing for dynamic measurements over time. The voxel size was set at 0.2 mm, the number of time samples at 2048, and the sampling rate at 31.25 MHz. Sound speed and density were assumed to be homogeneous, 1495 m/s and 994 kg/m^3 respectively. Acoustic attenuation was not assumed. Experimental and simulated measurement results are given in Figure 15, focusing on the 1101st to 1700th time samples. Both measurements exhibit similar shape at similar time samples. The output pattern occurred at a slightly later timestep in simulated results than in experimental results, an indication of discrepancy in sound speed distribution, and could be attributed to our assumption of acoustic homogeneity. The image assumed as the true initial pressure was reconstructed from experimental measurements using dynamic 3D PACT reconstruction, possibly resulting in appreciable discrepancies in structure and optical property distribution.

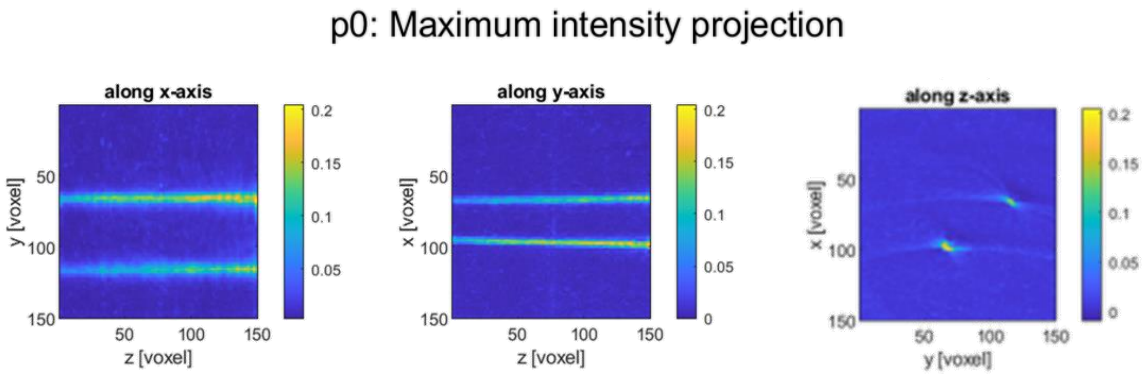

Figure 14 Initial pressure MIPs of tube phantom (360th frame) along x-axis (left), y-axis (middle), and z-axis (right).

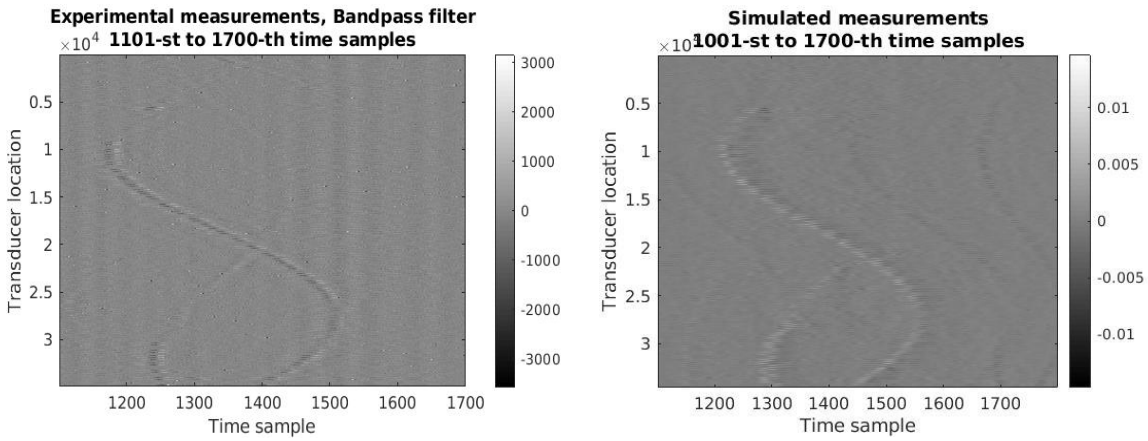

Figure 15 Experimental (left) and simulated (right) measurements from tube phantom over time. Both show 1101st to 1700th time samples. Experimental measurements were filtered using a bandpass filter with a frequency range of 500 kHz – 8 MHz.

5. Conclusion

In this thesis, we established a framework of dynamic PACT virtual imaging trials for small animals that includes generation of numerical mouse phantom, optical and acoustic property assignment, and simulations of photon transport and acoustic wave propagation. PACT VITs provide a method to facilitate the assessment and optimization of imaging systems and algorithms, while conducting clinical trials may be limited by monetary expense, time requirements, and ethical dilemmas. This framework allows for easy modification of parameters of the imaging system as well as the phantom of interest.

Mimicking the imaging geometry of the tabletop TriTom system, we simulated photon transport and produced simulated optical fluence output for the dynamic MOBY phantom. We subsequently simulated acoustic wave propagation, producing simulated pressure measurements at each transducer location outside the object over 2048 time samples. We also presented validation results for a static x-shaped phantom and a dynamic tube phantom, comparing simulated measurements with experimental measurements. Experimental results for both phantoms resembled their respective experimental measurements.

The proposed framework can be used to assess and optimize the existing imaging system. For example, the TriTom system provides light delivery of limited illumination views during an object scan at each tomographic view, as evident by simulated optical fluence outputs, which affects PACT image quality. Further investigation of the illumination geometry can be conducted by use of the framework to examine its impact of the PACT image quality.

The framework is currently limited by the memory capacity of the GPU used, restricting the grid size of simulation. For example, memory capacity of the GPUs that are currently available prevents the use of grids finer than 0.2 mm for the given measurement geometry. However, the development of such hardware has been accelerated, meaning in the near future a new GPU with larger memory will allow for VITs with finer simulation grids using this framework. For optically and acoustically realistic VITs using this framework, further research into realistic optical and acoustic properties of the object is needed.

References

[1] "Photoacoustic Computed Tomography (PACT)," *Computational Imaging Science Laboratory*. [Online]. Available: https://anastasio.bioengineering.illinois.edu/research/photoacoustic-computed-tomography-pact/. [Accessed: 08-Feb-2022].

[2] J. Poudel, Y. Lou, and M. A. Anastasio, "A survey of computational frameworks for solving the acoustic inverse problem in three-dimensional photoacoustic computed tomography," Physics in Medicine & Biology, vol. 64, no. 14, 2019.

[3] K. Wang and M. A. Anastasio, "Photoacoustic and thermoacoustic tomography: Image formation principles," *Handbook of Mathematical Methods in Imaging*, pp. 786–787, 2011.

[4] K. Wang, J. Xia, C. Li, L. V. Wang, and M. A. Anastasio, "Fast spatiotemporal image reconstruction based on low-rank matrix estimation for dynamic photoacoustic computed tomography," *Journal of Biomedical Optics*, vol. 19, no. 05, p. 1, 2014.

[5] L. J. Rich, E. R. Bolookat, and M. Seshadri, "Dynamic photoacoustic imaging of neurovascular coupling in salivary glands," *Journal of Oral Biosciences*, vol. 61, no. 4, pp. 236–241, 2019.

[6] E. Abadi, W. P. Segars, B. M. Tsui, P. E. Kinahan, N. Bottenus, A. F. Frangi, A. Maidment, J. Lo, and E. Samei, "Virtual clinical trials in medical imaging: A Review," *Journal of Medical Imaging*, vol. 7, no. 04, p. 1, 2020.

[7] A. D. McNaught, A. Wilkinson, and A. D. Jenkins, in *IUPAC compendium of Chemical Terminology: The gold book*, Research Triangle Park, NC: International Union of Pure and Applied Chemistry, 2006, pp. 409–409.

[8] G. Mettivier, A. Sarno, Y. Lai, B. Golosio, V. Fanti, M. E. Italiano, X. Jia, and P. Russo, "Virtual clinical trials in 2D and 3D X-ray breast imaging and dosimetry: Comparison of CPU-based and GPU-based Monte Carlo codes," *Cancers*, vol. 14, no. 4, p. 1027, 2022.

[9] F. di Franco, A. Sarno, G. Mettivier, A. M. Hernandez, K. Bliznakova, J. M. Boone, and P. Russo, "Geant4 Monte Carlo simulations for virtual clinical trials in breast X-ray imaging: Proof of concept," *Physica Medica*, vol. 74, pp. 133–142, 2020.

[10] R. Taschereau and A. F. Chatziioannou, "Monte Carlo simulations of absorbed dose in a mouse phantom from 18-fluorine compounds," *Medical Physics*, vol. 34, no. 3, pp. 1026–1036, 2007.

[11] B. van der Heyden, S. Roden, R. Dok, S. Nuyts, and E. Sterpin, "Virtual monoenergetic micro-ct imaging in mice with Artificial Intelligence," *Scientific Reports*, vol. 12, no. 1, 2022.

[12] Y. Tang and J. Yao, "3d Monte Carlo simulation of light distribution in mouse brain in quantitative photoacoustic computed tomography," *Quantitative Imaging in Medicine and Surgery*, vol. 11, no. 3, pp. 1046–1059, 2020.

[13] Y. Lou, W. Zhou, T. P. Matthews, C. M. Appleton, and M. A. Anastasio, “Generation of anatomically realistic numerical phantoms for photoacoustic and ultrasonic breast imaging,” *Journal of Biomedical Optics*, vol. 22, no. 4, p. 041015, 2017.

[14] “k-Wave,” *k-Wave A MATLAB toolbox for the time-domain simulation of acoustic wave fields*. [Online]. Available: http://www.k-wave.org/. [Accessed: 07-Feb-2022].

[15] Y. Wang, E. Helminen, and J. Jiang, “Building a virtual breast elastography Phantom lab using Open source software,” *2014 IEEE International Ultrasonics Symposium*, 2014.

[16] X. Song, G. Chen, A. Zhao, X. Liu, and J. Zeng, “Virtual optical-resolution photoacoustic microscopy using the K-Wave Method,” *Applied Optics*, vol. 60, no. 36, p. 11241, 2021.

[17] S. Agrawal, T. Suresh, A. Garikipati, A. Dangi, and S.-R. Kothapalli, “Modeling combined ultrasound and photoacoustic imaging: Simulations aiding device development and artificial intelligence,” *Photoacoustics*, vol. 24, p. 100304, 2021.

[18] F. Li, U. Villa, S. Park, S. He, and M. A. Anastasio, “A framework for ultrasound computed tomography virtual imaging trials that employs anatomically realistic numerical breast phantoms,” *Medical Imaging 2021: Ultrasonic Imaging and Tomography*, 2021.

[19] “MCXLAB: MCX for MATLAB and GNU Octave,” *MCXLAB: MCX for MATLAB and GNU Octave. Monte Carlo eXtreme: GPU-based Monte Carlo Simulations: Doc/MCXLAB*. [Online]. Available: http://mcx.space/wiki/index.cgi?Doc%2FMCXLAB. [Accessed: 07-Feb-2022].

[20] H. Wang, D. B. Stout, and A. F. Chatziioannou, “A deformable Atlas of the laboratory mouse,” *Molecular Imaging and Biology*, vol. 17, no. 1, pp. 18–28, 2014.

[21] W. SEGARS, “Development of a 4-D digital mouse phantom for molecular imaging research,” *Molecular Imaging & Biology*, vol. 6, no. 3, pp. 149–159, 2004.

[22] S. A. Ermilov, H.-P. F. Brecht, V. Ivanov, D. S. Dumani, S. Y. Emelianov, and M. A. Anastasio, “A 3D imaging system integrating photoacoustic and fluorescence orthogonal projections for anatomical, functional and molecular assessment of rodent models,” *Photons Plus Ultrasound: Imaging and Sensing 2018*, Mar. 2018.

[23] D. S. Dumani, H.-P. Brecht, V. Ivanov, M. A. Anastasio, J. R. Cook, S. A. Ermilov, S. Y. Emelianov, W. Thompson, and A. Yu, “Preclinical small animal imaging platform providing co-registered 3D maps of photoacoustic response and fluorescence,” *Photons Plus Ultrasound: Imaging and Sensing 2019*, Mar. 2019.

[24] W. F. Cheong, S. A. Prahl, and A. J. Welch, “A review of the optical properties of biological tissues,” *IEEE Journal of Quantum Electronics*, vol. 26, no. 12, pp. 2166–2185, Dec. 1990.

[25] G. Strangman, M. A. Franceschini, and D. A. Boas, “Factors affecting the accuracy of near-infrared spectroscopy concentration calculations for focal changes in Oxygenation Parameters,” *NeuroImage*, vol. 18, no. 4, pp. 865–879, 2003.

[26] "Digimouse Atlas FEM mesh," *Monte Carlo eXtreme: GPU-based Monte Carlo Simulations: MMC/DigimouseMesh. Section 6: Tissue optical properties.* [Online]. Available: http://mcx.space/wiki/index.cgi?MMC%2FDigimouseMesh. [Accessed: 07-Feb-2022].

[27] "Speed of sound," *Speed of Sound " IT'IS Foundation*. [Online]. Available: https://itis.swiss/virtual-population/tissue-properties/database/acoustic-properties/speed-of-sound/. [Accessed: 07-Feb-2022].

[28] "Density," *Density " IT'IS Foundation*. [Online]. Available: https://itis.swiss/virtual-population/tissue-properties/database/density/. [Accessed: 07-Feb-2022].

[29] "Attenuation constant," *Attenuation Constant " IT'IS Foundation*. [Online]. Available: https://itis.swiss/virtual-population/tissue-properties/database/acoustic-properties/attenuation-constant/. [Accessed: 07-Feb-2022].

[30] C. Bench, A. Hauptmann, and B. Cox, "Toward accurate quantitative photoacoustic imaging: Learning Vascular Blood Oxygen Saturation in three dimensions," *Journal of Biomedical Optics*, vol. 25, no. 08, p. 085003, 2020.

[31] S. G. Johnson, Notes on Perfectly Matched Layers (PMLs), 19-Jul-2008. [Online]. Available: https://klein.mit.edu/~stevenj/18.369/spring09/pml.pdf. [Accessed: 07-Feb-2022].

Appendix A Phantom Labeling Table

	MOBY	Mouse Atlas			Optical Properties			
Tissue Category	**Tissue**	**Tissue**	**Prev. label**	**Assigned label**	**Mu_A [mm^{-1}]**	**Mu_S [mm^{-1}]**	**Anisotropy (G)**	**Refrac. Index (N)**
Background	background	background	0	0	0.002	0	0.99	1.33
Body Background	Body (background)			1	0.0191	6.6	0.9	1.37
Skin	skin			2	0.0191	6.6	0.9	1.37
Glands	thyroid			3	0.024	8.9	0.9	1.37
		lachrymal_glands	12	4	0.024	8.9	0.9	1.37
Fat		brown_fat	24	5	0.024	8.9	0.9	1.37
		nasal_cavity	25	6	0.024	8.9	0.9	1.37
		abdominal_fat	26	7	0.024	8.9	0.9	1.37
		subcutaneous_fat	101	8	0.024	8.9	0.9	1.37
Other	lesn			9	0.024	8.9	0.9	1.37
	eyes	eyes	3	10	0.0026	0.01	0.9	1.37
		spinal_cord	200	11	0.0186	11.1	0.9	1.37
Heart	hrt_myoLV	left_ventricle	91	12	0.024	8.9	0.9	1.37
	hrt_myoRV	right_ventricle	93	13	0.024	8.9	0.9	1.37
	hrt_myoLA	left_atrium	94	14	0.024	8.9	0.9	1.37
	hrt_myoRA	right_atrium	95	15	0.024	8.9	0.9	1.37
	hrt_bldplLV			16	0.024	8.9	0.9	1.37
	hrt_bldplRV			17	0.024	8.9	0.9	1.37
	hrt_bldplLA			18	0.024	8.9	0.9	1.37
	hrt_bldplRA			19	0.024	8.9	0.9	1.37
		heart_wall	9	20	0.024	8.9	0.9	1.37
		main_aorta	96	21	0.024	8.9	0.9	1.37
Respiratory	lung	lungs	21	22	0.076	10.9	0.9	1.37
	airway			23	0.076	10.9	0.9	1.37
Urinary /Reproductive	bladder	urinary_bladder	13	24	0.024	8.9	0.9	1.37
	vas_def			25	0.024	8.9	0.9	1.37
	testicular	testis	14	26	0.024	8.9	0.9	1.37
Muscle		muscle	27	27	0.024	8.9	0.9	1.37
		masseter_muscles	11	28	0.024	8.9	0.9	1.37
Digestive	liver	liver	18	29	0.072	5.6	0.9	1.37
	gall_bladder	gall_bladder	22	30	0.072	5.6	0.9	1.37
	st_wall			31	0.024	8.9	0.9	1.37
	st_cnts	stomach	15	32	0.024	8.9	0.9	1.37
	pancreas			33	0.072	5.6	0.9	1.37
	kidney			34	0.05	5.4	0.9	1.37
		left_kidney	190	35	0.05	5.4	0.9	1.37

		right_kidney	191	36	0.05	5.4	0.9	1.37
	spleen	spleen	16	37	0.072	5.6	0.9	1.37
	sm_intest			38	0.024	8.9	0.9	1.37
	large_intest			39	0.024	8.9	0.9	1.37
		intestines	23	40	0.024	8.9	0.9	1.37
	li_air			41	0.0026	0.01	0.9	1.37
	si_air			42	0.0026	0.01	0.9	1.37
Brain	brain	rest_brain	10	43	0.0186	11.1	0.9	1.37
	cerebral_cortex	external_cerebrum	7	44	0.0186	11.1	0.9	1.37
	cerebellum	cerebellum	5	45	0.0186	11.1	0.9	1.37
	corpus_callosum			46	0.0186	11.1	0.9	1.37
	brainstem			47	0.0186	11.1	0.9	1.37
		medulla	4	48	0.0186	11.1	0.9	1.37
	striatum	striatum	8	49	0.0186	11.1	0.9	1.37
	thal			50	0.0186	11.1	0.9	1.37
	hippo			51	0.0186	11.1	0.9	1.37
	hypothalamus			52	0.0186	11.1	0.9	1.37
	amygdala			53	0.0186	11.1	0.9	1.37
	lateral_septal_nuclei_activity			54	0.0186	11.1	0.9	1.37
	anterior_commissure			55	0.0186	11.1	0.9	1.37
	anterior_pretectal_nucleus_activ			56	0.0186	11.1	0.9	1.37
	periaqueductal_gray			57	0.0186	11.1	0.9	1.37
	aqueduct			58	0.0186	11.1	0.9	1.37
	cerebral_peduncle			59	0.0186	11.1	0.9	1.37
	cochlear_nuclei			60	0.0186	11.1	0.9	1.37
	deep_mesencephalic_nuclei			61	0.0186	11.1	0.9	1.37
	fimbria			62	0.0186	11.1	0.9	1.37
	fornix			63	0.0186	11.1	0.9	1.37
	globus_pallidus			64	0.0186	11.1	0.9	1.37
	inferior_colliculus			65	0.0186	11.1	0.9	1.37
	internal_capsule			66	0.0186	11.1	0.9	1.37
	interpeduncular_nucleus			67	0.0186	11.1	0.9	1.37
	lateral_dorsal_nucleus_of_thalamus_actucleus_of_thalamus_activity			68	0.0186	11.1	0.9	1.37
	lateral_geniculate			69	0.0186	11.1	0.9	1.37
	lateral_lemniscus			70	0.0186	11.1	0.9	1.37
	medial_geniculate			71	0.0186	11.1	0.9	1.37
	nucleus_accumbens			72	0.0186	11.1	0.9	1.37
	olfactory_areas	olfactory_bulbs	6	73	0.0186	11.1	0.9	1.37
	optic_tract			74	0.0186	11.1	0.9	1.37
	pontine_gray			75	0.0186	11.1	0.9	1.37

	spinal_trigeminal_tract			76	0.0186	11.1	0.9	1.37
	substantia_nigra			77	0.0186	11.1	0.9	1.37
	superior_colliculus			78	0.0186	11.1	0.9	1.37
	pineal_gland			79	0.0186	11.1	0.9	1.37
	ventral_thalamic_nuclei			80	0.0186	11.1	0.9	1.37
	ventricular_system			81	0.0186	11.1	0.9	1.37
Bone	rib	ribs	302	82	0.0136	8.6	0.9	1.37
	skull	skull	301	83	0.0136	8.6	0.9	1.37
		pelvis	304	84	0.0136	8.6	0.9	1.37
	humerus			85	0.0136	8.6	0.9	1.37
	radius			86	0.0136	8.6	0.9	1.37
	ulna			87	0.0136	8.6	0.9	1.37
	femur			88	0.0136	8.6	0.9	1.37
	fibula			89	0.0136	8.6	0.9	1.37
	tibia			90	0.0136	8.6	0.9	1.37
	patella			91	0.0136	8.6	0.9	1.37
	bone (remaining)			92	0.0136	8.6	0.9	1.37
	marrow			93	0.0136	8.6	0.9	1.37
	spine			94	0.0136	8.6	0.9	1.37
		upper_hindlimb_left	305	95	0.0136	8.6	0.9	1.37
		lower_hindlimb_left	306	96	0.0136	8.6	0.9	1.37
		hindpaw_left	307	97	0.0136	8.6	0.9	1.37
		upper_hindlimb_right	308	98	0.0136	8.6	0.9	1.37
		lower_hindlimb_right	309	99	0.0136	8.6	0.9	1.37
		hindpaw_right	310	100	0.0136	8.6	0.9	1.37
		forepaw_left	311	101	0.0136	8.6	0.9	1.37
		lower_forelimb_left	312	102	0.0136	8.6	0.9	1.37
		upper_forelimb_left	313	103	0.0136	8.6	0.9	1.37
		forepaw_right	314	104	0.0136	8.6	0.9	1.37
		lower_forelimb_right	315	105	0.0136	8.6	0.9	1.37
		upper_forelimb_right	316	106	0.0136	8.6	0.9	1.37
		sternum	317	107	0.0136	8.6	0.9	1.37
		left_scapula	318	108	0.0136	8.6	0.9	1.37
		right_scapula	319	109	0.0136	8.6	0.9	1.37
		left_clavicle	320	110	0.0136	8.6	0.9	1.37
		right_clavicle	321	111	0.0136	8.6	0.9	1.37
		vertebra_1 - 35	201	112	0.0136	8.6	0.9	1.37